# Sensitive Superconducting Gravity Gradiometer Constructed with Levitated Test Masses

C. E. Griggs,[1] M. V. Moody,[1] R. S. Norton,[1] H. J. Paik,[1] and K. Venkateswara[2]
[1]*Department of Physics, University of Maryland, College Park, Maryland 20742, USA*
[2]*Center for Experimental Nuclear Physics and Astrophysics, University of Washington, Seattle, Washington 98195, USA*

(Received 28 February 2017; revised manuscript received 21 September 2017; published 21 December 2017)

We demonstrate basic operations of a two-component superconducting gravity gradiometer (SGG) that is constructed with a pair of magnetically levitated test masses coupled to superconducting quantum-interference devices. A design that gives a potential sensitivity of $1.4 \times 10^{-4}$ E $\mathrm{Hz}^{-1/2}$ (1 E $\equiv 10^{-9}$ $\mathrm{s}^{-2}$) in the frequency band of 1 to 50 mHz and better than $2 \times 10^{-5}$ E $\mathrm{Hz}^{-1/2}$ between 0.1 and 1 mHz for a compact tensor SGG that fits within a 22-cm-diameter sphere. The SGG has the capability of rejecting the platform acceleration and jitter in all 6 degrees of freedom to one part in $10^9$. Such an instrument has applications in precision tests of fundamental laws of physics, earthquake early warning, and gravity mapping of Earth and the planets.

DOI: 10.1103/PhysRevApplied.8.064024

## I. INTRODUCTION AND BACKGROUND

Precise gravity measurements are required to study the fundamental nature of gravitation. Measurements of gravity can also provide a better understanding of Earth and the planets, help find natural resources, and improve inertial navigation and surveying. To distinguish gravity from platform accelerations, the equivalence principle requires a *differential* measurement. A gravity gradiometer detects a spatial derivative of the gravitational field and ideally is immune to the vibrations of the platform.

Several versions of the superconducting gravity gradiometer (SGG) have been developed at the University of Maryland (UM) with support from NASA and other funding agencies [1–3]. A three-axis diagonal-component SGG with a baseline of 19 cm and *mechanically suspended* test masses reached a performance level of 0.02 E $\mathrm{Hz}^{-1/2}$ [1 E $\equiv 10^{-9}$ $\mathrm{s}^{-2}$, E (eötvös) is a unit of gravity gradient] in the laboratory, which is 3 orders of magnitude more sensitive than demonstrated to date by other gradiometers, including atom-interferometer gravity gradiometers [4–7]. The SGG was used to set the best limit of Newton's inverse-square law (ISL) at 1 m, at the level of two parts in $10^4$ [8]. An off-diagonal SGG was also developed for an airborne application [9].

*Time-variable* gravity measurements from space are essential to address the causes and consequences of climate change [10]. The satellite-to-satellite tracking (SST) mission, Gravity Recovery and Climate Experiment (GRACE), proved the importance of global gravimetric measurements from satellites to observe and understand mass transports driven by climatic, tectonic, and anthropogenic forces [11]. The first space-borne gradiometer, Gravity Field and Steady-State Ocean Circulation Explorer (GOCE) [12], demonstrated that satellite gradiometer data can substantially advance our knowledge of the *static* gravity field to higher spatial resolution [13].

To improve our knowledge of the gravity field for Earth and the planets to beyond that achieved by other missions, we are developing a more sensitive SGG based on *levitated* test masses [14]. By replacing the relatively stiff mechanical springs used to suspend the test masses in the earlier devices with soft magnetic levitation, the sensitivity of the SGG can be improved by 2 to 3 orders of magnitude. A levitation scheme, which simplifies the design and construction of the advanced SGG, was demonstrated [15]. We construct and test a prototype *two-component* SGG based on this levitation scheme and demonstrate common-mode (CM) rejection, the most essential characteristic of a SGG.

Unlike SST, where the gravity signal is deduced from orbital motions of two satellites, a gradiometer directly measures the gravitational field over a short baseline within a spacecraft. In addition, the SGG measurements have *full 3D* observability and are not limited to along-track observations, as in the case of the SST system [16]. A very attractive feature of the SGG is the *tunability* of the measurement band and sensitivity *in flight* by changing its resonance frequency, which allows measurements of both static and time-variable gravity fields from the same mission (see Fig. 9). Decade-long gravity missions require space-qualified cryocoolers. A 4-K cryocooler has already flown on the International Space Station [17], and other cryocoolers with negligible vibration levels are under development [18–20].

In this paper, we discuss the design and operating principle of the SGG, report a demonstration of the SGG constructed with levitated test masses, and compute its potential sensitivity. We also discuss the applications of the SGG technology in Earth and planetary sciences as well as in fundamental physics.

 

## II. DESIGN AND OPERATING PRINCIPLE OF THE SGG

### A. Principle of gravity gradiometry

The second spatial derivatives of the gravitational potential $\phi(x_i, t)$ form a gravity gradient tensor $\Gamma_{ij}$:

$$\Gamma_{ij} \equiv -\frac{\partial^2 \phi}{\partial x_i \partial x_j}. \tag{1}$$

$\Gamma_{ij}$ is symmetric, and its trace is proportional to the local mass density $\rho$ due to the ISL:

$$\sum_i \Gamma_{ij} = -\nabla^2 \phi = 4\pi G\rho. \tag{2}$$

This constraint leaves *five* independent components for the tensor: two diagonal and three off diagonal. A *diagonal*-component gradiometer can be constructed by differencing signals between two *linear* accelerometers whose sensitive axes are aligned along their line of sight. Likewise, an *off-diagonal*-component gradiometer can be constructed by differencing signals between two concentric *angular* accelerometers whose moment arms are orthogonal to each other.

In a diagonal-component gradiometer, linear and angular accelerations of the platform couple to the gradiometer through departures from parallelism and concentricity of the sensitive axes of the accelerometers, respectively [1]. There are like error sources in an off-diagonal-component device. A departure of the rotation axes from parallelism provides coupling to angular acceleration, and an asymmetric mass distribution in each moment arm causes linear acceleration to couple to the gradiometer [9]. For a review of superconducting accelerometry and gravity gradiometry, see Ref. [21].

### B. SGG with levitated test masses

#### 1. Levitation scheme

A magnetically levitated mass requires 5 or 6 degrees-of-freedom (d.o.f.) control, which generally requires levitation coils of elaborate design [22]. A simple levitation scheme, which provides stiff suspension for unwanted d.o.f. while permitting complete compliance along and about the sensitive axis, has been devised and demonstrated at UM (see Appendix A).

Figure 1 illustrates the principle of levitation by a current induced along a superconducting tube. Inside the levitation tube, each of $N$-turn wires carries current $I_L$. This induces a screening current on the tube $NI_L$ to flow along the inner surface of the tube and return along the outer surface. The current density on the outer surface is *uniform*, independent of the current distribution inside the tube. This generates a *cylindrically symmetric* magnetic field, which falls off as $1/r$, as shown in Fig. 1(a). A tube-shaped superconducting test mass with a larger diameter surrounds the levitation tube. When the test mass is concentric with the levitation tube, the field is uniform around the levitation tube and does not exert a net force on the test mass. However, if the test mass is displaced radially, as shown in Fig. 1(b), the field becomes stronger at $P$ and weaker at $Q$, resulting in a radial restoring force.

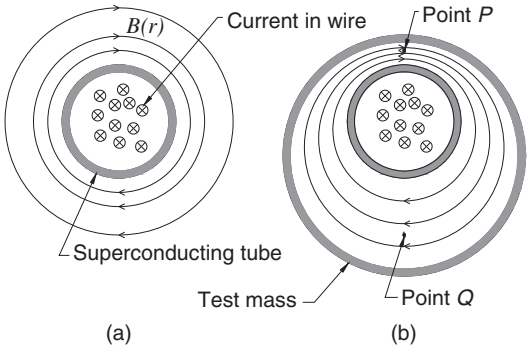


FIG. 1. Principle of levitation by current induced on a superconducting tube. (a) In the absence of a test mass, the current induced on the levitation tube generates a cylindrically symmetric magnetic field. (b) A tube-shaped superconducting test mass with a larger diameter surrounds the levitation tube. If the test mass is displaced radially, the field becomes stronger at $P$ and weaker at $Q$, resulting in a radial restoring force.

#### 2. Two-component SGG

A prototype *two-component* SGG with levitated test masses has been constructed and tested [14]. The guiding principle in designing the SGG for laboratory test is the capability to levitate the test masses in 1 $g$. The required 1 $g$ operation leads to a test mass design using thin vanes to produce a light mass ($m = 0.10$ kg). Figure 2 is a perspective view of two niobium (Nb) test masses levitated by a current along a single horizontal Nb tube. Each test mass has two wings 180° apart, which provide a moment arm about the tube axis ($x$). A balancing screw is provided at the end of each wing to adjust the center-of-mass (c.m.) position and bring it to the rotation axis. The current flowing along the tube provides stiff suspension in the radial directions ($y$ and $z$) but leaves the test masses to

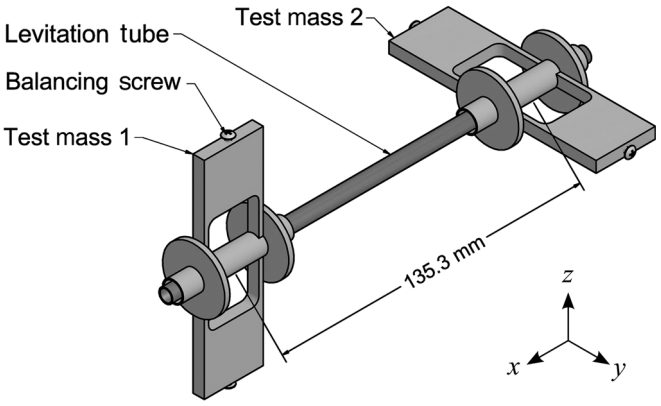


FIG. 2. Two superconducting test masses levitated around a single superconducting tube.

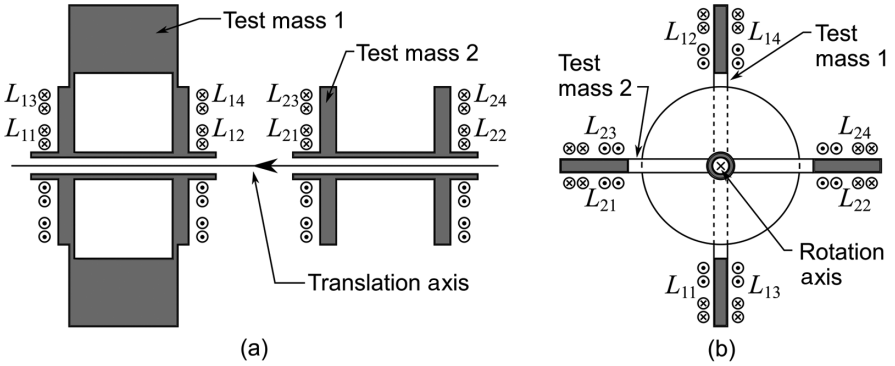


FIG. 3. Test mass and sensing coil configuration for (a) the diagonal-component and (b) the off-diagonal-component SGG.

translate freely along the axis and rotate freely about the same axis.

On the ground, still a large levitation current ($NI_L \sim 10^3$ A) is required to levitate the test masses against Earth's gravity, and the SGG suffers $g$-related errors, such as sensitivity to tilt. In $0\,g$, the levitation and alignment can be achieved with much smaller currents and $g$-related errors disappear; thus, it should be much easier to reach the intrinsic noise level of the SGG.

Figure 3 shows the test mass and sensing coil configuration for the SGG. For the diagonal component, pancake-shaped Nb coils $L_{ij}(i = 1, 2; j = 1, \ldots, 4)$ are placed near the disk faces of the test masses to detect their translational motion, as shown in Fig. 3(a). For the off-diagonal component, pancake-shaped coils $L_{ij}$ are located near the rectangular surfaces of the test masses to detect their rotational motion, as shown in Fig. 3(b).

Figure 4(a) is the gradient sensing circuit of the diagonal component. Persistent currents $I_1$ and $I_2$ are stored in the superconducting loops formed by $L_{11}$ and $L_{12}$, and by $L_{21}$ and $L_{22}$, respectively. The linear acceleration signals from the two test masses are differenced in the superconducting quantum-interference device (SQUID) to detect gravity gradient $\Gamma_{xx}$. In an ideal gradiometer with perfectly matched test masses and sensing coils, setting $I_1 = I_2$ gives perfect rejection of the CM in the differential-mode (DM) output. In a real device, there are mismatches, and $I_2/I_1$ is adjusted to maximize the CM rejection ratio (CMRR). Figure 4(b) is the CM sensing circuit. With the sense of $I_2$ reversed, the linear acceleration signals are summed in the SQUID to detect linear acceleration $a_x$.

Circuit diagrams for off-diagonal-component gradient $\Gamma_{yz}$ and angular acceleration $\alpha_x$ are identical to those in Figs. 4(a) and 4(b). The rotation of test masses 1 and 2 modulates the corresponding inductances in the same way as the translation of the test masses in Figs. 4(a) and 4(b).

### 3. Scale factor and null stability

Signal differencing by means of stable persistent currents *before* detection is a feature of the SGG. This assures excellent *null stability* of the device, which, in turn, improves the overall CM rejection. Further, the SQUID sees only a small differential signal, thereby reducing the dynamic range requirement on the amplifier and signal-processing electronics. The mechanical stability of the materials at cryogenic temperatures guarantees that misalignments are also stable. These error coefficients can, therefore, be measured once and for all during the initial setup, multiplied by the proper acceleration components, and subtracted from the gradiometer output. By applying this "residual CM balance" [23], the acceleration error coefficients are reduced effectively to $\leq 10^{-7}$ and $\leq 10^{-9}$ for the diagonal and off-diagonal components, respectively, in our previous devices [3,9].

The SGG is a *completely passive* system. Because of the extreme stability of persistent currents and the mechanical stability of materials at low temperatures, once persistent currents are stored in the levitation and sensing coils, the positions and orientations of the test masses with respect to the coils, as well as the accelerometer scale factors, remain constant. Hence, there is nothing to control actively, except for the temperature. This greatly simplifies the design and operation of the SGG.

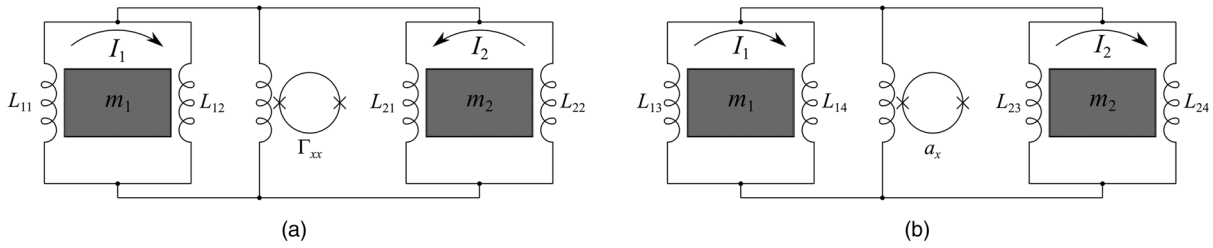


FIG. 4. (a) Gravity gradient and (b) linear acceleration sensing circuit of the diagonal-component SGG.

## III. INSTRUMENT NOISE AND ERRORS OF THE SGG

### A. Intrinsic instrument noise

The instrument noise power spectral density (PSD) limit set by thermal force noise and readout noise for a diagonal component is given by

$$S_\Gamma(f) = \frac{8}{m\ell^2}\left[k_B T\frac{\omega_D}{Q_D} + \frac{(\omega^2-\omega_D^2)^2}{2\beta\eta\omega_D^2}E_A(f)\right], \quad (3)$$

where $m$ and $\ell$ are the mass of each test mass and the gradiometer baseline, $\omega_D$ and $Q_D$ are the (angular) resonance frequency and $Q$ of the DM, $\beta$ and $\eta$ are the electromechanical energy coupling and energy coupling efficiency from circuit to SQUID, and $E_A(f)$ is the energy resolution of the SQUID at signal frequency $f$, respectively. The instrument noise PSD for an off-diagonal component is given by

$$S_\Gamma(f) = \frac{2}{\xi^2 J}\left[k_B T\frac{\omega_D}{Q_D} + \frac{(\omega^2-\omega_D^2)^2}{2\beta\eta\omega_D^2}E_A(f)\right], \quad (4)$$

where $\xi$ is the gradient-to-angular-acceleration conversion factor, and $J$ is the moment of inertia of the rotating arm. Equations (3) and (4) are generalized from those derived by Chan *et al.* [2] and by Moody *et al.* [24] to allow $f_D < f$.

In the SGG with mechanically suspended test masses, $\beta$ is given by

$$\beta = \frac{k_e}{k_e + k_m}, \quad (5)$$

where $k_e$ and $k_m$ are the electrical and mechanical spring constants, respectively. In the SGG with levitated test masses, $k_m = 0$; therefore, $\beta$ should be unity. In practice, the levitation field may provide parasitic stiffness causing $\beta < 1$, which must be investigated. The circuit energy coupling efficiency $\eta$ is given by

$$\eta = \frac{L_i}{L_p + L_i}, \quad (6)$$

where $L_p \equiv (L_{11}^{-1} + L_{12}^{-1} + L_{21}^{-1} + L_{22}^{-1})^{-1}$ is the parallel combination of the four sensing coil inductances, and $L_i$ is the inductance of the SQUID input coil. For our earlier models of SGG, $S_\Gamma(f)$ was dominated by the SQUID noise. In the present device, $S_\Gamma^{1/2}(f)$ is reduced by over 2 orders of magnitude by replacing the stiff mechanical spring ($f_D \sim 10$ Hz) with a soft magnetic spring ($f_D \leq 0.1$ Hz).

Table I summarizes the design parameters of our prototype SGG. Substituting these values along with $T = 4.2$ K and $E_A(f) = (1 + 0.1\ \text{Hz}/f)5\times10^{-31}\ \text{J Hz}^{-1}$ (commercial dc SQUID) into Eqs. (3) and (4), we find $S_\Gamma^{1/2}(f) = 1.4\times10^{-4}\,\text{E Hz}^{-1/2}$ for the diagonal components and $3.5\times10^{-4}\ \text{E Hz}^{-1/2}$ for the off-diagonal components in the frequency band of 1 to 50 mHz. Below $10^{-3}$ Hz, the SGG exhibits a $1/f$ power noise. The sensitivity of this compact SGG exceeds that of the much larger SGG with mechanically suspended test masses by 2 orders of magnitude.

TABLE I. SGG design parameters.

| Parameter | Diagonal | Off diagonal |
|---|---|---|
| $m$ (kg) | 0.10 | |
| $\ell$ (m) | 0.135 | |
| $J$ (kg m$^2$) | | $8.1\times10^{-5}$ |
| $\xi$ | | 0.96 |
| $f_C$ (Hz) | 0.1 | 0.1 |
| $Q_C$ | $10^4$ | $10^4$ |
| $f_D$ (Hz) | 0.02 | 0.02 |
| $Q_D$ | $2\times10^6$ | $2\times10^6$ |
| $\beta$ | 1 | 1 |
| $\eta$ | 0.4 | 0.4 |

### B. Temperature sensitivity

The enhanced displacement-to-acceleration sensitivity (by $\omega_D^2$) gives another important advantage: reduced sensitivity to temperature change. Because of the dependence of the superconducting penetration depth on the temperature, the SGG is sensitive to temperature fluctuations through the modulation of sensing coil inductances [1]. For the SGG to reach the $3\times10^{-5}\ \text{E Hz}^{-1/2}$ sensitivity, the temperature needs to be controlled to $2\times10^{-5}\ \text{K Hz}^{-1/2}$, well within the capability of germanium thermometers. Although the gradient sensitivity increases by 2 orders of magnitude from that of the mechanically suspended SGG, the temperature control becomes easier by an order of magnitude [3].

### C. Patch fields

Electrostatic patch fields apply parasitic forces to the test masses. The resolution of the Gravity Probe B (GPB) mission was severely compromised by this error [25]. The patch effect is also an important error source for the LISA test masses [26]. However, unlike GPB and LISA, which require disturbance-free gyros or reference masses, the SGG uses test masses suspended with relatively stiff magnetic springs from the spacecraft. This implies that the residual motion of the test masses is small relative to the gap; hence, the spatial variability of patch fields is less of a concern. However, the nonlinear modulation of the gap produces acceleration noise that cannot be removed by the CM balance. The patch fields will also interact with the fluctuating charge of the isolated test mass. This error will lead to a charge control requirement.

Here, we estimate the noise generated by modulation of the patch fields on the diagonal component $\Gamma_{xx}$. The test mass response to the platform acceleration in the radial

direction is negligible due to the very stiff (>10-Hz) radial suspension provided by the levitation current. The platform acceleration $a_p(\omega)$ along the sensitive axis causes the test mass to be displaced with respect to the sensing coils by $x(\omega) = a_p(\omega)/(\omega^2 - \omega_C{}^2)$, where $\omega_C$ is the CM (angular) resonance frequency. The patch potentials produce a force gradient [27] given by

$$\frac{\partial F}{\partial x} = \kappa \frac{\varepsilon_0 A v^2}{d^3}, \tag{7}$$

where $A$ is the area, $\varepsilon_0$ is the permittivity of vacuum, $v$ is the rms potential fluctuation, $d$ is the gap, and $\kappa$ is a dimensionless constant between $-1.2$ and $-1.8$, depending on the assumed form of the voltage distribution. Substituting $d + x$ into $d$, expanding, and integrating over $x$, we find

$$F = F_0 + \frac{\kappa\varepsilon_0 A v^2}{d^3} x - \frac{3}{2}\frac{\kappa\varepsilon_0 A v^2}{d^4} x^2 + O\left(\left(\frac{x}{d}\right)^3\right). \tag{8}$$

The first-order term modifies the CM spring constant:

$$k = m\omega_C^2 - \frac{\kappa\varepsilon_0 A v^2}{d^3}. \tag{9}$$

The second-order term represents the nonlinear coupling to the platform noise. By dividing platform acceleration PSD $S_a(f)$ by the CM frequency response function and Fourier transforming, we obtain the autocorrelation function of displacement $R_x(\tau)$. By Fourier transforming $[R_x(\tau)]^2$ again with the aid of Eq. (8), we find the gravity gradient noise PSD due to the patch fields:

$$S_{\Gamma,\mathrm{PF}}(f) = \int_{-\infty}^{\infty} d\tau e^{-i2\pi f\tau}\left[\frac{1}{2\pi}\int_{-\infty}^{\infty} df' \frac{3}{2}\frac{\kappa\varepsilon_0 A v^2}{m\ell d^4}\frac{1}{(2\pi)^4}\frac{S_a(f')}{(f_C^2 - f'^2 + if_C f'/Q_C)^2} e^{i2\pi f'\tau}\right]^2. \tag{10}$$

By evaluating the $f'$ and $\tau$ integrals, we obtain

$$S_{\Gamma,\mathrm{PF}}(f) = \left[\frac{3}{2}\frac{\kappa\varepsilon_0 A v^2}{m\ell d^4}\frac{S_a(f_C)}{(2\pi)^5}\frac{1}{2f_C^2}\right]^2 \frac{2\pi Q_C}{f_C}\frac{1}{(f - 2f_C)^2 + (2f_C/Q_C)^2}. \tag{11}$$

$S_{\Gamma,\mathrm{PF}}(f)$ peaks at $f = 2f_C$ and becomes a white noise at $f$ sufficiently far away from $2f_C$. We expect that the patch potentials will produce similar errors for the off-diagonal-component channels.

For high-purity Nb with which the test masses are constructed, $v = 0.33$ V [28]. With the parameter values listed in Table I as well as $A = 5 \times 10^{-4}$ m$^2$ and $d = 5 \times 10^{-4}$ m into Eq. (9), we find $k = (0.16 + 8 \times 10^{-6})$ N m$^{-1}$. This small modification of the spring constant is inconsequential since the spring constants of the two test masses are matched precisely in the CM balancing procedure. Substituting the parameter values and $S_a(0.1\ \mathrm{Hz}) = 1 \times 10^{-15}$ m$^2$ s$^{-4}$ Hz$^{-1}$ into Eq. (11), we obtain $S_{\Gamma,\mathrm{PF}}^{1/2}(f) = 3 \times 10^{-5}$ E Hz$^{-1/2}$ at $f = 0.01$ Hz. This is smaller than the scale factor nonlinearity error by a factor of 3. We aim to reduce the nonlinearity errors by 2 orders of magnitude by measuring and compensating for the nonlinear response of the instrument (see Table II).

### D. Other noise and errors

Many other types of noise must be suppressed for the SGG to reach the intrinsic instrument noise limit. To eliminate coupling to the external magnetic fields, a $\mu$-metal shield is provided for the cryostat, and the superconducting circuit is completely shielded in a superconductor. The SGG platform needs to be sufficiently rigid for its own thermal noise to be negligible and to allow a high degree of CM balance. The techniques to mitigate these noise and other errors of the instrument have been studied extensively and documented [2,3].

TABLE II. Expected errors of the diagonal-component channels in the ground laboratory at 0.01 Hz.

| Error source | Ambient level | Coupling compensation | Error |
|---|---|---|---|
| Linear acceleration | $1 \times 10^{-8}$ m s$^{-2}$ Hz$^{-1/2}$ | $(1 \times 10^{-5})(1 \times 10^{-4})$ | $1.3 \times 10^{-7}$ E Hz$^{-1/2}$ |
| Angular acceleration | $3 \times 10^{-9}$ rad s$^{-2}$ Hz$^{-1/2}$ | $(1 \times 10^{-5})(1 \times 10^{-4})$ | $5 \times 10^{-9}$ E Hz$^{-1/2}$ |
| Angular rate | $5 \times 10^{-8}$ rad s$^{-1}$ Hz$^{-1/2}$ | $(7 \times 10^{-5}$ rad s$^{-1})(1 \times 10^{-4})$ | $5 \times 10^{-7}$ E Hz$^{-1/2}$ |
| Attitude | $8 \times 10^{-7}$ rad Hz$^{-1/2}$ | $(73$ s$^{-2})(1 \times 10^{-5})(1 \times 10^{-4})$ | $6 \times 10^{-5}$ E Hz$^{-1/2}$ |
| Scale factor nonlinearity | $1 \times 10^{-14}$ m$^2$ s$^{-4}$ Hz$^{-1}$ | $(90$ m$^{-2}$ s$^2$ Hz$^{1/2})(1 \times 10^{-2})$ | $9 \times 10^{-6}$ E Hz$^{-1/2}$ |
| Patch field nonlinearity | $1 \times 10^{-14}$ m$^2$ s$^{-4}$ Hz$^{-1}$ | $(30$ m$^{-2}$ s$^2$ Hz$^{1/2})(1 \times 10^{-2})$ | $3 \times 10^{-6}$ E Hz$^{-1/2}$ |
| Temperature fluctuations | $2 \times 10^{-5}$ K Hz$^{-1/2}$ | $(1.5$ E K$^{-1})(1 \times 10^{-2})$ | $3 \times 10^{-7}$ E Hz$^{-1/2}$ |

Table II lists the major errors (in addition to the intrinsic noise) of the diagonal-component channels of the prototype SGG in the ground laboratory. The off-diagonal-component channels have similar errors. The third column shows the coupling constant to various types of environment noise times the degree of compensation applied. The angular rate error multiplied by Earth's spin rate produces centrifugal acceleration error. The attitude error modulates Earth's gravity gradient as well as gravity field $g_E$. In the SGG orientation chosen (two axes horizontal and one axis vertical), the gravity gradient error becomes a second-order error and is negligible. The scale factor nonlinearity error is computed by assuming the same nonlinearity coefficient in the displacement as in our mechanically suspended SGG. The linear acceleration PSD caused by the attitude error is entered as the ambient level for both types of nonlinearity errors. The SGG has sufficient rejection and compensation capability to keep each error below the intrinsic noise level.

## IV. CONSTRUCTION AND TEST OF THE SGG

### A. Construction of two-component SGG

Each test mass is constructed by snugly fitting a Nb tube into a precision hole drilled through the central axis of the test mass body. For ease of winding the levitation coil, two separate levitation tubes are used, one for each test mass, instead of using a common levitation tube for the pair as shown in Fig. 2. Each levitation coil is wound with 160 turns of Nb wire, 40 turns on each quadrant of the levitation tube. The return wires are routed on the outside of a superconducting shield enclosing the test mass and sensing coils to prevent the magnetic field arising from the current in the returning wires from canceling that produced by the levitation current.

Figure 5 shows our prototype SGG mounted on the cryostat. The cross-shaped housing facing the front is one of the two Nb housings for the two test masses. The other one (hidden from view) is mounted on the opposite face of a precision titanium (Ti) cube, 10.2 cm per side. The Ti cube is polished to make the surfaces parallel or perpendicular to two parts in $10^5$.

### B. Dynamics of levitated test masses

The test masses are levitated with $NI_L = 1.1 \times 10^3$ A. To free the test masses, we have to apply a relatively large asymmetric current in the rotation sensing coils since mass balance has not been applied to the test masses yet. With the rotation sensing coils dedicated to freeing the test masses, it is not possible to demonstrate the off-diagonal-component SGG.

Our model indicates that the c.m. of one test mass is offset by 80 $\mu$m away from the rotation axis, which is consistent with the machining precision of the prototype SGG. This c.m. offset will be reduced to $<1$ $\mu$m by adjusting the balancing screws iteratively (see Fig. 2). At

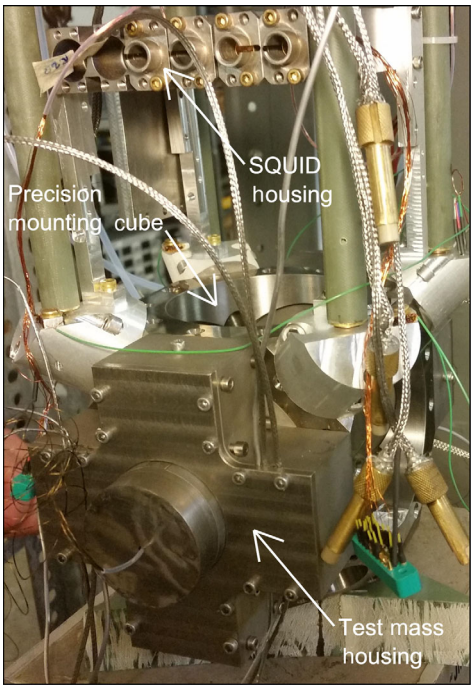


FIG. 5. Two-component SGG mounted on the cryostat.

the pressure $<10^{-6}$ torr, the translational mode exhibits $Q$ of $3.6 \times 10^4$, which is quite remarkable for a single mass with no CM balance.

Figure 6 shows the observed resonance frequency squared versus the sensing current squared for the translational mode of one test mass. The excellent fit of the data points to a straight line shows that the acceleration-to-current transfer function is *highly linear*. The nonzero $y$ intercept corresponding to 1.4 Hz, however, indicates that there is parasitic stiffness. A similar plot for the rotational mode does not show such stiffness. The parasitic stiffness in the translational mode appears to be coming from coupling of the levitation current to the translation d.o.f. For a detailed discussion, see Appendix B.

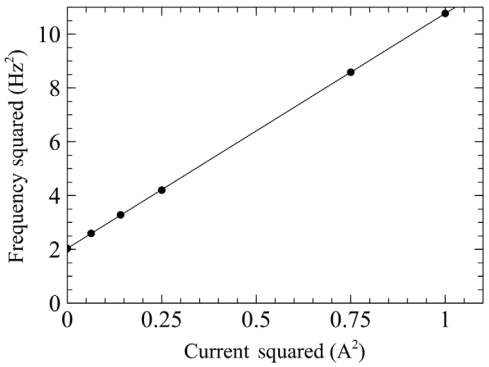


FIG. 6. Frequency squared vs current squared for the translational mode.

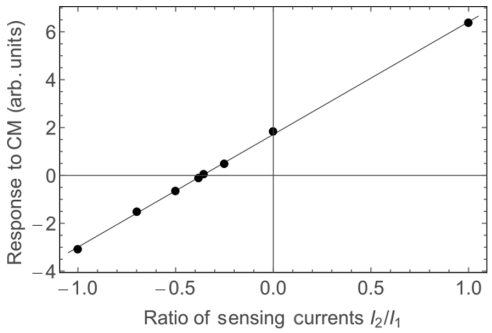


FIG. 7. CM acceleration to SQUID transfer function versus the ratio of sensing currents.

### C. Common mode balance

A characteristic of a SGG is its ability to balance out the CM sensitivity by adjusting persistent currents, thus, achieving extreme null stability. This is demonstrated in our SGG. Figure 7 shows the SQUID response to an applied CM acceleration plotted against the ratio of the sensing currents in the two accelerometers. The CM balance is achieved with the current ratio of $I_2/I_1 = -0.37$.

Without a provision to measure linear and angular accelerations in the other two axes, the CMRR in this device is limited to $10^3$ due to misalignment of the sensitive axes. This limited CMRR does not permit demonstration of the sensitivity of the SGG since the DM output is dominated by uncompensated dynamic noise of the laboratory.

## V. FUTURE MODIFICATIONS AND IMPROVEMENTS

### A. Elimination of parasitic stiffness

As shown in Appendix B, the parasitic stiffness is caused by magnetic fields produced by screening currents on the outer surface of the test masses induced by the strong levitation field. We find a simple solution to eliminate the parasitic stiffness. We insert a thin insulating layer between the center tube and the rest of the test mass body, thus, prevent the screening currents from coupling to the translational motion.

### B. Mass balance and sensitive axis alignment

Our CMRR goal for the SGG is $10^9$ by combining an initial balance to one part in $10^5$ with persistent currents and alignments, and a residual balance to one part in $10^4$. To meet this goal, the mass balance of the test masses must be improved by a factor of 100. We plan to improve the balance of the test masses at room temperature by a factor of 10 by trimming the mass. The remaining factor of 10 improvement will be achieved by iteratively adjusting the balancing screws and testing the balance at 4.2 K.

The alignment of the levitation tubes is limited to $10^{-3}$ rad in our prototype SGG. To achieve the initial balance to one part in $10^5$, alignment must be improved to $10^{-5}$ rad. We investigate the possibility of implementing an *in situ* axis alignment system by using the cryogenically proven PiezoKnobs manufactured by Janssen Precision Engineering [29]. These piezoknobs have a minimum step of 1–5 nm at 4 K and can potentially provide $10^{-7}$-rad alignment.

### C. Tensor SGG

We plan to expand the SGG to a *full tensor* instrument. Figure 8 is a partially exploded view of our future tensor SGG. Six identical accelerometers are mounted on the Ti mounting cube. The entire SGG assembly will weigh 12 kg and fit within a sphere of 22 cm in diameter.

The device will measure all six components of the *gradient tensor*, as well as all six components of the linear and angular accelerations of *the platform*. The acceleration components will be used to achieve the overall CMRR of $10^9$.

### D. Expected sensitivity of the spaceborne SGG

For Earth science missions, the SGG will be scaled up to $m = 1.0$ kg and $\ell = 0.20$ m to improve the sensitivity by a factor of 5 over the values computed above. Figure 9 shows the intrinsic noise spectral densities $S_\Gamma^{1/2}(f)$ for two different values of $f_D$. With $f_D$ tuned to 20 mHz, the SGG will have a wide bandwidth up to 0.05 Hz, permitting a high spatial resolution of gravity. With $f_D$ tuned to 0.2 mHz, the sensitivity below 1 mHz will be improved by an order of

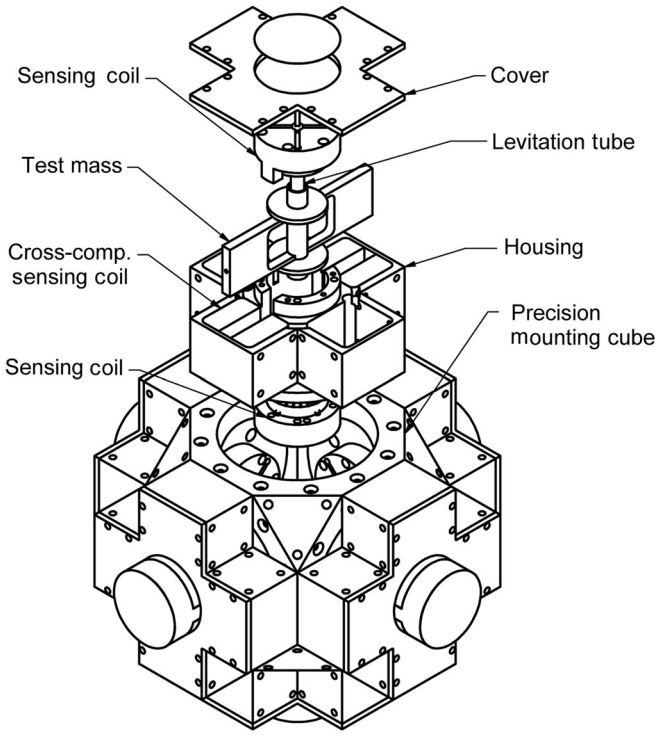


FIG. 8. Partially enlarged view of the tensor SGG.

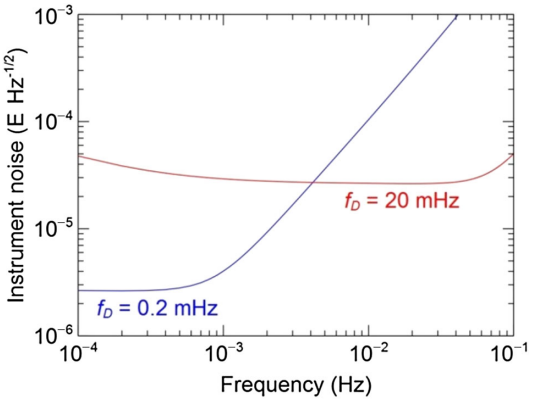


FIG. 9. Intrinsic noise of SGG for Earth science missions. The red and blue curves represent the instrument noise corresponding to $f_D = 20$ and 0.2 mHz, respectively.

magnitude. The sensitivities indicated by the red and blue curves correspond to 2 to 3 orders of magnitude improvement over those achieved by GOCE [30] and GRACE [13], respectively. The typical acceleration level encountered in a low-Earth orbit $1 \times 10^{-6}$ m s$^{-2}$ Hz$^{-1/2}$ will produce a gradient error of $8.7 \times 10^{-6}$ E Hz$^{-1/2}$, 1 order of magnitude below the target sensitivity of the SGG for Earth gravity missions. In $0\,g$, the attitude modulation of gravity field, which is the largest error in the ground laboratory, is absent. If the spacecraft vibrations and jitter are controlled to within 10 times above the levels of the ground laboratory listed in Table II, the CMRR of $10^9$ will make drag-free control unnecessary, except in the along-track direction as in GOCE.

It is interesting to compare the expected sensitivity of our spaceborne SGG with the demonstrated sensitivity of the LISA Pathfinder (LPF) [26]. The LPF test masses weighed 1.93 kg each. Between 0.7 and 20 mHz, LPF reached differential acceleration noise of $5.6 \times 10^{-15}$ m s$^{-2}$ Hz$^{-1/2}$, which corresponds to $2.8 \times 10^{-5}$ E Hz$^{-1/2}$ when divided by the SGG baseline, $\ell = 0.20$ m. This is basically identical to the sensitivity of the SGG tuned to $f_D =$ 20 mHz (red curve in Fig. 9). It is remarkable that LPF achieved this sensitivity at room temperature with test masses only twice as heavy as those of the SGG. However, to achieve this sensitivity, LPF was sent to the first Lagrange point ($L1$), about $1.5 \times 10^6$ km from Earth and had to be in a drag-free satellite. The SGG does not require a full drag-free satellite. Its sensitivity below 1 mHz improves by an order of magnitude if $f_D$ be tuned to 0.2 mHz. The SGG sensitivity can be improved further by using a two-stage SQUID with proven lower noise [31]. So, the SGG can potentially reach sensitivity 2 orders of magnitude beyond that achieved by LPF.

## VI. CONCLUSION AND DISCUSSION

Highly sensitive SGGs were developed at UM in the 1980s and early 1990s. The first gradiometer developed at UM in the early 1980s demonstrated a gradient resolution of 0.7 E Hz$^{-1/2}$ [2], a level yet to be surpassed by a room-temperature device on Earth. A later version has demonstrated CM rejection to better than one part in $10^7$, which led to a demonstrated noise level of 0.02 E Hz$^{-1/2}$ [3]. The SGG has the capability of rejecting CM accelerations to one part in $10^7$ or better, owing to the extreme stability of persistent currents combined with mechanical stability of the platform at cryogenic temperatures.

While convenient for ground-based testing, mechanical springs reduce the inherent sensitivity of the SGG. By replacing the relatively stiff mechanical springs used in the earlier devices with soft magnetic levitation, the sensitivity of the device can be improved by 2 to 3 orders of magnitude. We design, construct, and test a prototype two-component SGG, one diagonal and one off diagonal, by combining a pair of levitated test masses, each with 2 d.o.f. Both masses are successfully levitated, and CM rejection is demonstrated with levitated test masses. We find parasitic stiffness in the diagonal-component channel due to the magnetic field produced by the levitation current coupling to the translational motion. We are able to identify the cause of the problem and find a way to eliminate this stiffness by a straightforward modification of the test masses.

For NASA's Earth science and planetary science applications, we plan to construct a full tensor SGG by combining six levitated test masses [14,32]. A compact design with each test mass weighing 0.10 kg and a baseline of 0.135 m yields an intrinsic noise level of $1.4 \times 10^{-4}$ E Hz$^{-1/2}$ for the diagonal components and $3.5 \times 10^{-4}$ E Hz$^{-1/2}$ for the off-diagonal components in the frequency band of 1 to 50 mHz. This represents over 2 orders of magnitude improvement beyond what has been demonstrated with the much larger SGG with mechanically suspended test masses. The measurement bandwidth and sensitivity of the SGG can be tuned in flight to detect both *static* and *time-variable* gravity fields from *the same mission* [14]. The SGG mission will be like GRACE and GOCE combined, with the sensitivity improved by 2 to 3 orders of magnitude in all frequencies.

Sensitive SGGs with levitated test masses will find useful applications in many precision gravity experiments, such as a satellite test of the equivalence principle [22] and detection of gravitomagnetic fields in Earth orbit [33]. A scaled-up version of the tensor SGG can detect transient gravity signals from an earthquake rupture at the speed of light. A network of such detectors can determine the magnitude and the epicenter of the earthquake and issue a more prompt warning of the earthquake than is possible with a seismometer network [34,35].

The present ground-based laser interferometer GW detectors cover a frequency band from 10 Hz to several kilohertz [36], whereas a future space mission like LISA will cover from 0.1 mHz to 0.1 Hz [37]. Recently, a type of

ground-based GW detector called SOGRO (Superconducting Omni-directional Gravitational Radiation Observatory) was proposed to cover a midfrequency band of 0.1 to 10 Hz [38]. SOGRO is basically an enormously scaled-up version of the tensor SGG to a baseline of 30–50 m with each test mass weighing 5 tons, The target sensitivity of SOGRO is $10^{-20}$ $\mathrm{Hz}^{-1/2}$.

The absolute stability of the superconducting sensing circuit, which utilizes flux quantization, and the enhanced stability of the mechanical platform at cryogenic temperatures render the SGG the capability of rejecting the platform vibrations to one part in $10^9$ or better. This gives the SGG a tremendous advantage over other systems in detecting tiny gravity signals at low frequencies ($f < 1$ Hz), where vibration isolation becomes extremely difficult. These advantages will be fully utilized in gravity-mapping missions for Earth and the planets and in the proposed SOGRO detector.

## ACKNOWLEDGMENTS

We acknowledge useful discussions with Peter Shawhan, Frank Lemoine, David Rowlands, Xiaoyi Li, Shin-Chan Han, Hyung Mok Lee, Jan Harms, Runqiu Liu, and Xing Bian. We appreciate technical support from Keith Burghardt as an undergraduate helper. This work is partly supported by NASA Grants No. NNX12AK18G and No. NNX14AI43G and NSF Grant No. PHY1105030.

## APPENDIX A: LEVITATION BY CURRENT ALONG A TUBE

### 1. Levitation force and resonance frequency

Consider an inner superconducting tube (levitation tube) of radius $R_1$ with wires inside it carrying a net current $I$ and an outer superconducting tube (test mass) of radius $R_2$. When the tubes are centered, the surface currents on the inner tube are distributed such that the magnetic field outside it is uniformly centered about the tube from Ampere's law, as in Fig. 1(a), regardless of the location of the wires within the tube. However, if the outer tube is displaced, as shown in Fig. 1(b), the magnetic field above the inner levitating tube is compressed, while the field below it is expanded. This provides a restoring force on the outer tube.

To estimate the restoring force, we use the image current method since the Lorentz force between two current-carrying wires obeys the same equation as the Coulomb force between two line charges (except for the sign). From electrostatics [39], we know that the equipotentials between two equal and opposite line charges are circular cylinders. The force between the two tubes is the same as the force between the line current inside the levitating tube and its image current. The location of the tubes and the line currents is shown schematically in Fig. 10. Solving for the equipotential between two line charges separated by a distance $2a$, we obtain the following relations:

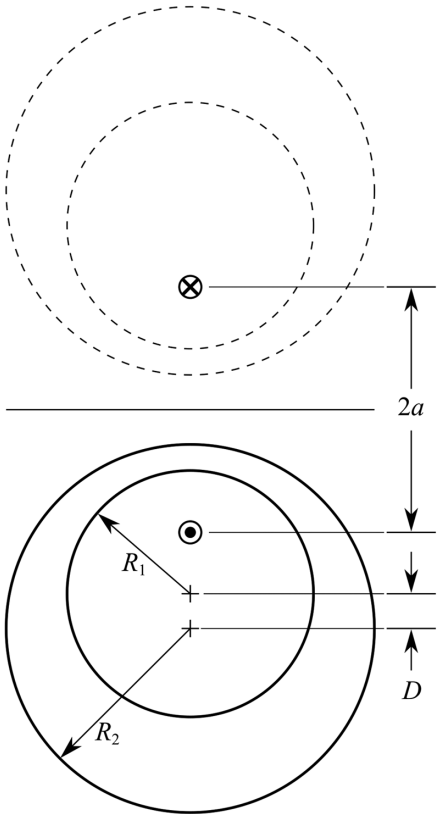


FIG. 10. Schematic of the test mass and levitation tube.

$$R_1 = a\,\mathrm{csch}U_1, \qquad R_2 = a\,\mathrm{csch}U_2,$$
$$D = a(\coth U_1 - \coth U_2), \tag{A1}$$

$$U_1 = 2\pi\varepsilon_0 V/\lambda, \tag{A2}$$

where $V$ is the potential, and $\lambda$ is the line charge per unit length. Combining these equations, we get

$$D = (R_2^2 + a^2)^{1/2} - (R_1^2 + a^2)^{1/2}. \tag{A3}$$

The force between two currents separated by a distance $2a$ can be expressed as

$$F_r = \frac{\mu_0}{2\pi}\frac{I^2}{2a}l, \tag{A4}$$

where $l$ is the length of the outer tube (i.e., test mass). For the case where the two cylinders are nearly concentric, we have $D \ll R_1, R_2$. Equations (A3) and (A4) then yield

$$a = \frac{R_2^2 - R_1^2}{2D}, \tag{A5}$$

$$F_r = \frac{\mu_0}{2\pi}\frac{I^2}{R_2^2 - R_1^2}Dl. \tag{A6}$$

This method establishes the spring constant and, hence, the frequency of the radial oscillation of the test mass in $0\,g$,

where the test mass is concentric with respect to the levitation tube. Dividing by the mass of the test mass $m$ gives the radial resonance frequency:

$$\omega_r^2 = \frac{\mu_0}{2\pi}\frac{I^2}{R_2^2 - R_1^2}\frac{l}{m}. \tag{A7}$$

Now, we consider the case where the test mass sags with respect to the levitation tube due to gravity. When the levitating tube rests horizontally on the earth, the outer tube is initially at rest on top of it. As the levitation current is increased, it experiences a repulsive force and begins to rise above the levitating tube and approaches the concentric position as the current goes to infinity. When the two cylinders are not concentric, the equations of force have to be solved to obtain the restoring force:

$$F_r = \frac{\mu_0}{2\pi}\frac{I^2}{R_2^2 - R_1^2} Dl = mg. \tag{A8}$$

The general form of the solution for the distance between the tubes can be expressed as

$$D = \left[R_2^2 + \left(\frac{\mu_0}{4\pi}\frac{lI^2}{mg}\right)^2\right]^{1/2} - \left[R_1^2 + \left(\frac{\mu_0}{4\pi}\frac{lI^2}{mg}\right)^2\right]^{1/2}. \tag{A9}$$

As the test mass is a free rigid body, it will have 6 d.o.f. It should have three linear modes and three angular modes, which are all distinct. To calculate the frequencies of the linear modes of the test mass, we invoke the principle of flux conservation in the levitating coil:

$$\Phi_0 = (L_T + L_S)I_L = L_L I_L, \tag{A10}$$

where $L_T$ is the inductance due to the magnetic field between the two tubes, $L_S$ is the stray inductance arising from the field elsewhere, $L_L$ is the total inductance of the levitation coil, and $I_L$ is the persistent current in the coil ($I = NI_L$). To calculate the frequency of the vertical mode, we need to express the inductance in terms of the separation $D$ between the centers of the test mass and the levitating tube. This can be done by calculating the magnetic flux in the region between the tubes as

$$L_T I_L = l\int_0^D B dz. \tag{A11}$$

The field can once again be calculated using the image current method described earlier. We get

$$L_T = \frac{\mu_0 l}{2\pi}\ln\left[\frac{(r_0 + D)(2a - r_0)}{(2a - r_0 - D)r_0}\right], \tag{A12}$$

where

$$r_0 = R - \left[a\coth\left(\operatorname{csch}^{-1}\frac{R_1}{a}\right) + a\right]. \tag{A13}$$

The total stored energy can be expressed as

$$E = \frac{\Phi_0^2}{2L_L}. \tag{A14}$$

The restoring force and the spring constant are given by

$$F_v = -\frac{dE}{dD} = -\frac{\Phi_0^2}{2L_L^2}\frac{dL_L}{dD}, \tag{A15}$$

$$k_v = \frac{dF_v}{dD} = \frac{\Phi_0^2}{2L_L^2}\left[\frac{2}{L_L}\left(\frac{dL_T}{dD}\right)^2 - \frac{d^2L_T}{dD^2}\right], \tag{A16}$$

using the fact that $L_S$ is not modulated by $D$. Substituting $\Phi_0 = L_L I_L$, we get

$$\omega_v^2 = \frac{k_v}{m} = \frac{I_L^2}{2m}\left[\frac{2}{L_L}\left(\frac{dL_T}{dD}\right)^2 - \frac{d^2L_T}{dD^2}\right]. \tag{A17}$$

The vertical mode frequency of the test mass is $f_v = \omega_v/2\pi$.

### 2. Demonstration of levitation scheme

To test this levitation principle, we develop the simple setup shown in Fig. 11. A Nb tube of 4.78 mm o.d. is used as the levitating tube. The test mass consists of a Nb tube of 6.35 mm o.d., 12.7 mm length, and 0.38-mm wall thickness, weighing 0.78 g. Since there is no magnetic restoring force along a straight levitation tube, we introduce a slight curvature in the levitating tube to have gravity provide the restoring force as in a pendulum. A Nb wire is looped through the levitating tube 49 times ($N = 49$). A small pancake coil located beneath the test mass is connected to a SQUID to sense its motion.

As $I_L$ increases to 1.8 A (total levitation current: $NI_L = 88$ A), there appear two low-frequency modes and several high-frequency modes. In particular, the lowest

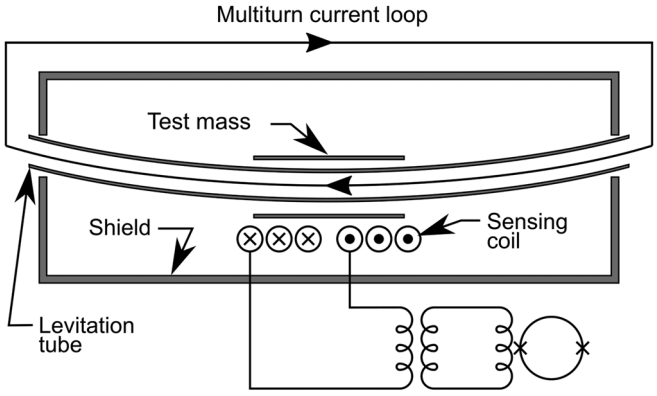


FIG. 11. Test setup for levitation scheme.

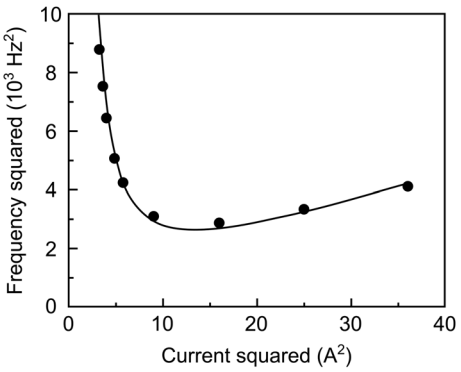


FIG. 12. Vertical mode frequency squared versus levitation current squared.

observed frequency, 0.34 Hz, agrees with the expected frequency of the sliding mode, in which the test mass slides along the levitating tube and is trapped in the gravitational potential well created by the curvature of the tube. Figure 12 shows $f_v^2$ versus $I_L^2$. The line represents the 2D model derived in Appendix A 1 and is computed numerically using Eq. (A17). It is remarkable how well the experiment agrees with our simple theory. When the test mass is barely levitated, $f_v$ is very high (approximately 100 Hz), since the magnetic field above the levitation tube [point $P$ in Fig. 1(b)] is much stronger than below (point $Q$). As $I_L$ increases to 3.5 A ($NI_L \sim 170$ A), $f_v$ is reduced to a minimum (approximately 50 Hz) because the magnetic field becomes more uniform around the levitation tube as the test mass becomes more concentric with the levitation tube. With a continued increase of $I_L$, $f_v$ increases again as the magnetic field increases everywhere.

Equation (A12) yields $L_T = 0.42$ $\mu$H for $D = 0.36$ mm, and $L_S = 0.05$ $\mu$H is obtained from our best fit of the data. However, the values of $L_T$ and $L_S$ are expected to change substantially in a more realistic 3D model.

## APPENDIX B: PARASITIC STIFFNESS AGAINST TRANSLATIONAL MOTION

### 1. Origin of parasitic stiffness

The magnetic field from the levitation current induces a current that flows along the inner surface of the central tube of the test mass and returns through the outer surface of the test mass. Figure 13(a) shows the current (blue) that flows through the outer surface of the test mass and the resulting magnetic field (red). Figure 13(b) shows the side (cross-sectional) view of the magnetic field that wraps around the center tube and the two wings. On the outer surface of the test mass, the current splits into three paths: one along the center tube and the other two to the two wings. The magnitude of the current along each path should be inversely proportional to the inductance of that path. Each wing is connected to the center tube by two narrow bridges $(w_b \times h \times r_b)$.

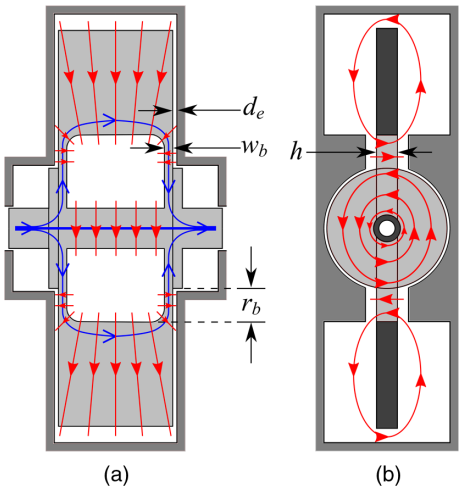


FIG. 13. Induced current on the test mass surfaces and the resulting magnetic fields.

The observed parasitic stiffness against the translational mode appears to arise mainly from the strong magnetic field that wraps around the narrow bridges. Because of the current continuity, the current that flows out across one bridge must be the same as the current that flows in across the other bridge. If the test mass undergoes a translational motion $x$ along the tube axis, the gap between the two edges of the test mass and the superconducting shield is modulated in the opposite direction: $d_e \pm x$, so the *total inductance* of the bridge-wing-bridge path, thus, the current along that path, will not change to the first order. However, the magnetic fields are modulated in the opposite directions in the two gaps, and, therefore, they must produce a net restoring force.

Let a fraction $\eta$ of the total current $I$ cross one bridge: $I_b = \eta I_L$. The magnetic field produced by this current in close proximity to the bridge can be estimated from Ampere's law:

$$\oint \overrightarrow{B_b} \cdot \overrightarrow{d\ell} = B_b(2h + 2w_b) = \mu_0 \eta I, \tag{B1}$$

where $w_b$ is the width of bridge, and $h$ is the height of the bridge. From Eq. (B1), we obtain

$$B_b = \frac{\mu_0 \eta I}{2(h + w_b)}. \tag{B2}$$

As the test mass is displaced, $B_b$ is modulated by $\delta B_b = \pm B_b(x/d_e)$ producing a restoring force:

$$F(x) = \frac{1}{2\mu_0}\left[B_b^2\left(1 - \frac{x}{d_e}\right)^2 - B_b^2\left(1 + \frac{x}{d_e}\right)^2\right]A = -\frac{2B_b^2 A}{\mu_0 d_e}x, \tag{B3}$$

where $A = 2r_b h$ and $r_b$ is the length of the bridge. From $F(x) = -m\omega_t^2 x$,

$$\omega_t^2 = \frac{2B_b^2 A}{\mu_0 m d_e} = \left[\frac{\mu_0 \eta I}{2(h+w_b)}\right]^2 \frac{2A}{\mu_0 m d_e}, \tag{B4}$$

$$f_t = \frac{1}{2\pi}\frac{\eta I}{h+w_b}\left(\frac{\mu_0 A}{2md_e}\right)^{1/2}. \tag{B5}$$

With numerical values $\eta \approx 0.2$, $I = 1200$ A, $h = 0.51$ cm, $w_b = 0.20$ cm, $r_b = 0.4$ cm, $d_e = 0.23$ cm, $A = 2r_b h = 0.41$ cm$^2$, and $m = 0.1$ kg, we find $f_r \approx 1.8$ Hz. This is very close to our observed frequency.

### 2. Hardware modification to eliminate parasitic stiffness

The original test mass is constructed by snugly fitting a Nb tube into a precision hole drilled through the central axis of the Nb test mass (see Fig. 2). One simple solution to eliminate the parasitic stiffness is to insert a thin insulating layer between the center tube and the rest of the test mass body. This prevents the returning currents on the outside of the test mass from branching to the two wings through the narrow bridges, thus, eliminating the strong magnetic field that wraps around the narrow bridges. Elimination of parasitic stiffness is one of the modifications being made to improve the performance of our SGG.


[1] H. A. Chan and H. J. Paik, Superconducting gravity gradiometer for sensitive gravity measurements. I. Theory, Phys. Rev. D **35**, 3551 (1987).

[2] H. A. Chan, M. V. Moody, and H. J. Paik, Superconducting gravity gradiometer for sensitive gravity measurements. II. Experiment, Phys. Rev. D **35**, 3572 (1987).

[3] M. V. Moody, H. J. Paik, and E. R. Canavan, Three-axis superconducting gravity gradiometer for sensitive gravity experiments, Rev. Sci. Instrum. **73**, 3957 (2002).

[4] N. Yu, J. M. Kohel, J. R. Kellogg, and L. Maleki, Development of an atom-interferometer gravity gradiometer for gravity measurements from space, Appl. Phys. B **84**, 647 (2006).

[5] H. Müller, S.-W. Chiow, S. Herrmann, S. Chu, and K. Y. Chung, Atom Interferometer Tests of the Isotrophy of Post-Newtonian Gravity, Phys. Rev. Lett. **100**, 031101 (2008).

[6] F. Sorrentino, Q. Bodart, L. Cacciapuoti, Y.-H. Lien, M. Prevedelli, G. Rosi, L. Salvi, and G. M. Tino, Sensitivity limits of a Raman atom interferometer as a gravity gradiometer, Phys. Rev. A **89**, 023607 (2014).

[7] G. W. Biedermann, X. Wu, L. Deslauriers, S. Roy, C. Mahadeswaraswamy, and M. A. Kasevich, Testing gravity with cold-atom interferometers, Phys. Rev. A **91**, 033629 (2015).

[8] M. V. Moody and H. J. Paik, Gauss's Law Test of Gravity at Short Range, Phys. Rev. Lett. **70**, 1195 (1993).

[9] M. V. Moody, A superconducting gravity gradiometer for measurements from a moving vehicle, Rev. Sci. Instrum. **82**, 094501 (2011).

[10] NASA, http://science.nasa.gov/earth-science/.

[11] B. D. Tapley, S. Bettadpur, J. C. Ries, P. F. Thompson, and M. M. Watkins, GRACE measurements of mass variability in the Earth system, Science **305**, 503 (2004).

[12] M. R. Drinkwater, R. Floberghagen, R. Haagmans, D. Muzi, and A. Popescu, *Earth Gravity Field from Space—From Sensors to Earth Sciences* (Kluwer, Dordrecht, 2003), Vol. 18, pp. 419–432.

[13] R. Pail, H. Goiginger, W.-D. Schuh, E. Höck, J. M. Brockmann, T. Fecher, T. Gruber, T. Mayer-Gürr, J. Kusche, A. Jäggi, and D. Rieser, Combined satellite gravity field model GOCO01S derived from GOCE and GRACE, Geophys. Res. Lett. **37**, L20314 (2010).

[14] C. E. Griggs, H. J. Paik, M. V. Moody, S.-C. Han, D. D. Rowlands, F. G. Lemoine, P. J. Shirron, and X. Li, Tunable superconducting gravity gradiometer for Mars climate, atmosphere, and gravity field investigation, in *Proceedings of the 46th Lunar and Planetary Science Conference, Houston, TX, 2015* (2015) [http://www.hou.usra.edu/meetings/lpsc2015/pdf/1735.pdf].

[15] K. Burghardt, Undergraduate thesis, University of Maryland, 2012.

[16] R. Rummel, W. Yi, and C. Stummer, GOCE gravitational gradiometry, J. Geodes. **85**, 777 (2011).

[17] H. Sugita, Y. Sato, T. Nakagawa, H. Murakami, H. Kaneda, K. Enya, M. Murakami, S. Tsunematsu, M. Hirabayashi SPICA Working Group, Development of mechanical cryocoolers for the Japanese IR space telescope SPICA, Cryogenics **48**, 258 (2008).

[18] D. Durand, J. Raab, R. Colbert, M. Michaelian, T. Nguyen, P. Petach, and E. Tward, NGST Advanced Cryocooler Technology Development Program (ACTDP) cooler system, AIP Conf. Proc. **823**, 615 (2006).

[19] J. J. Breedlove, K. J. Cragin, and M. V. Zagarola, Testing of a two-stage 10 K turbo-Brayton cryocooler for space applications, in *Proceedings of the 18th International Cryocooler Conference*, edited by S. D. Miller and R. G. Ross, Jr. (ICC Press, Boulder, CO, 2014), pp. 445–452.

[20] K. Cragin, K. Rule, and M. Zagarola, Characterization of emitted vibration from turbo-Brayton cryocoolers, in *Proceedings of the 19th International Cryocooler Conference*, edited by S. D. Miller and R. G. Ross, Jr. (ICC Press, Boulder, CO, 2016), pp. 471–478.

[21] H. J. Paik, in *SQUID Handbook*, edited by J. Clarke and A. Braginski (Wiley, New York, 2006), Vol. 2, Chap. 15, pp. 545–579.

[22] H. J. Paik, J.-P. Blaser, and S. Vitale, Principle of the STEP accelerometer design, Adv. Space Res. **32**, 1325 (2003).

[23] M. V. Moody, H. A. Chan, and H. J. Paik, Superconducting gravity gradiometer for terrestrial and space applications, J. Appl. Phys. **60**, 4308 (1986).

[24] M. V. Moody, H. J. Paik, and E. R. Canavan, Principle and performance of a superconducting angular accelerometer, Rev. Sci. Instrum. **74**, 1310 (2003).

[25] C. W. F. Everitt *et al.*, Gravity Probe B: Final Results of a Space Experiment to Test General Relativity, Phys. Rev. Lett. **106**, 221101 (2011).

[26] M. Armano *et al.*, Sub-Femto-*g* Free Fall for Space-Based Gravitational Wave Observatories: LISA Pathfinder Results, Phys. Rev. Lett. **116**, 231101 (2016).

[27] C. C. Speake, Forces and force gradients due to patch fields and contact-potential differences, Classical Quantum Gravity **13**, A291 (1996).

[28] *CRC Handbook of Chemistry and Physics*, 97th ed., edited by W. M. Haynes (CRC Press, Boca Raton, FL, 2016), pp. 12–119.

[29] www.janssenprecisionengineering.com.

[30] R. Floberghagen, M. Fehringer, D. Lamarre, D. Muzi, B. Frommknecht, C. Steiger, J. Piñeiro, and A. da Costa, Mission design, operation and exploitation of the gravity field and steady-state ocean circulation explorer mission, J. Geodes. **85**, 749 (2011).

[31] P. Falferi, M. Bonaldi, A. Cavalleri, M. Cerdonio, A. Vinante, R. Mezzena, K. Xu, G. A. Prodi, and S. Vitale, Noise sources and dissipation mechanisms of a $120\,\hbar$ SQUID amplifier, Appl. Phys. Lett. **82**, 931 (2003).

[32] X. Li, F. G. Lemoine, H. J. Paik, M. Zagarola, P. J. Shirron, C. E. Griggs, M. V. Moody, and S.-C. Han, Design of superconducting gravity gradiometer cryogenic system for Mars mission, in *Proceedings of the 19th International Cryocooler Conference* edited by S. D. Miller and R. G. Ross, Jr. (ICC Press, Boulder, CO, 2016), pp. 585–593.

[33] B. Mashhoon, H. J. Paik, and C. M. Will, Detection of the gravitomagnetic field using an orbiting superconducting gravity gradiometer. I. Theoretical principles, Phys. Rev. D **39**, 2825 (1989).

[34] J. Harms, J. P. Ampuero, M. Barsuglia, E. Chassande-Mottin, J.-P. Montagner, S. N. Somala, and B. F. Whiting, Transient gravity perturbations induced by earthquake rupture, Geophys. J. Int. **201**, 1416 (2015).

[35] J.-P. Montagner, K. Juhel, M. Barsuglia, J.-P. Ampuero, E. Chassande-Mottin, J. Harms, B. Whiting, P. Bernard, E. Clevede, and P. Lognonne, Prompt gravity signal induced by the 2011 Tohoku-Oki earthquake, Nat. Commun. **7**, 13349 (2016).

[36] G. Cella and A. Giazotto, Invited review article: Interferometric gravity wave detectors, Rev. Sci. Instrum. **82**, 101101 (2011).

[37] LISA Consortium, LISA: Laser Interferometer Space Antenna, https://www.lisamission.org/proposal/LISA.pdf.

[38] H. J. Paik, C. E. Griggs, M. V. Moody, K. Venkateswara, H. M. Lee, A. B. Nielsen, E. Majorana, and J. Harms, Low-frequency terrestrial tensor gravitational-wave detector, Classical Quantum Gravity **33**, 075003 (2016).

[39] J. D. Jackson, *Electrodynamics*, 3rd ed. (Wiley, New York, 1999), Chap. 2.